Constriction of cone-beam artifacts by the Z-smart reconstruction method

Frank Dennerlein, *Graduate Student Member, IEEE,* Frédéric Noo, *Member, IEEE,* Wolfgang Härer, Joachim Hornegger, and Günter Lauritsch

***Abstract*— We introduce a novel approach for 3D image reconstruction from CB data acquired along a full circular trajectory. Our approach, which we refer to as the Z-smart reconstruction method, follows the scheme of 1D filtering and 3D backprojection, while providing flexibility in the choice of the filtering directions. This flexibility allows us to modify the appearance of CB artifacts in the reconstruction results, so that, for certain imaging tasks, the Z-smart method can yield image quality that is significantly superior to that achievable with most other reconstruction algorithms for the full-scan circular trajectory. In particular, when imaging objects that have strong but localized heterogeneities in the axial direction, the Z-smart method can outperform both, the popular filtered-backprojection approach of Feldkamp *et al.*, and also ART, i.e. a fully 3D iterative reconstruction method. We provide a numerical evaluation of our algorithm using simulated CB data of an analytically defined tube phantom, with and without added noise.**

I. Introduction

Circular cone-beam (CB) computed tomography is an attractive method for medical imaging and also non-destructive testing because circular motion of the source-detector assembly is easy to implement, is mechanically robust, and allows fast data acquisition. Unfortunately, CB projections on a circular trajectory do not form a complete data set and thus prevent accurate and stable reconstruction [1], [2]. More specifically, accurate reconstruction may in general be performed only with significant sensitivity to data noise, and the only way to obtain results that are stable in the presence of practical noise levels is to sacrifice accuracy.

An attractive analytical reconstruction formula that allows numerically robust reconstruction for a full circular scan is the algorithm of Feldkamp, Davis and Kress [3], which we will refer to as FDK throughout this paper. The FDK algorithm uses simple 1D filtering and 3D backprojection steps and is theoretically well-supported in terms of 3D Radon transform theory. However, since the circular CB data is incomplete and the FDK method is approximate, it does not in general produce accurate reconstructions. It produces results with CB artifacts that are dependent on the magnitude with which the density function to be reconstructed varies in axial direction. Typically, these artifacts spread over wide regions of the reconstructed volume, even when the strong axial density variations are very localized within the object.

In this paper, we introduce the novel, analytical Z-smart reconstruction approach that is capable of producing, in certain scenarios, results of quality significantly superior to that of FDK. In particular, a remarkable reduction of CB artifacts can be achieved when imaging objects that contain strong but localized density variations in the axial direction. The Z-smart method consists, similar to FDK, of a filtering step and backprojection step. It requires, however, the selection of two parameters that impact the direction of the filtering lines required for reconstruction. We suggest a specific choice of these parameters and evaluate the performance of the resulting CB reconstruction algorithm using computer-simulated data.

This paper is structured as follows. Section II describes the full-scan acquisition geometry and the notation used throughout this article. In section III, we introduce the Z-smart reconstruction formula for the circular full-scan. Its behavior in terms of CB artifacts is described in section IV. We then suggest a specific selection of filter parameters for the Z-smart reconstruction algorithm in section V. A numerical evaluation of the suggested algorithm follows in section VI, where reconstruction results are compared to those of FDK, but also to those of a fully 3D iterative reconstruction method (ART). Conclusions and discussions terminate the main body of this paper in Sec. VII.

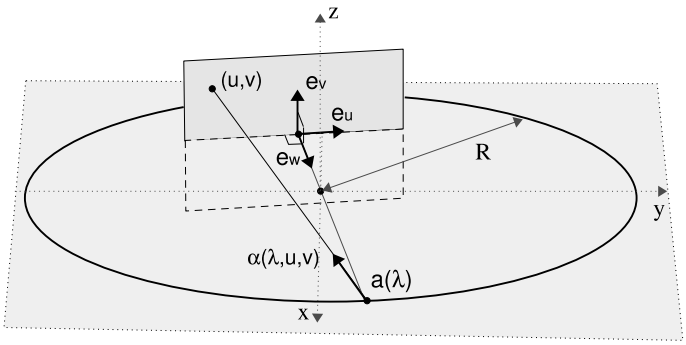

Fig. 1. Illustration of the full-scan circular CB data acquisition geometry assumed throughout this paper.

Manuscript received May 11, 2007. This work was partially supported by a grant of Siemens AG, Medical Solutions and by the U.S. National Institutes of Health (NIH) under grant R01 EB000627. Its contents are solely the responsibility of the authors and do not necessarily represent the official views of the NIH.

F. Dennerlein (fdenner@ucair.med.utah.edu) and F. Noo are with the Department of Radiology (UCAIR), University of Utah, Salt Lake City, UT, USA.

W. Härer and G. Lauritsch are with Siemens AG, Medical Solutions, Forchheim, Germany.

J. Hornegger is with the Institute of Pattern Recognition, University of Erlangen-Nuremberg, Erlangen, Germany.

II. Acquisition Geometry

In the following, we use the conventional notation to specify locations in space with vectors $\mathbf{x} = (x, y, z)^{\mathrm{T}}$, where x, y and z are the coordinates of a Cartesian world coordinate system and $^{\mathrm{T}}$ is the transpose operator. Without loss of generality, the coordinate z is measured along the rotation axis of the scanner, while coordinates x and y give positions within the slices orthogonal to the z-axis. We assume furthermore that during the scan, the X-ray source and the detector perform together a single, full rotation around the object under investigation so that the focal spot of the X-ray source describes a closed circle of radius R within the plane $z = 0$. The circular source trajectory can then be parametrized as

$$\mathbf{a}(\lambda) = (R\cos\lambda, R\sin\lambda, 0)^{\mathrm{T}} \tag{1}$$

with the polar angle of the source, λ, varying in $[0, 2\pi)$. In the following, we consider a planar detector geometry, which can be beneficially described using the orthonormal system of vectors

$$\begin{aligned} \mathbf{e}_u(\lambda) &= (-\sin\lambda, \cos\lambda, 0)^{\mathrm{T}} \\ \mathbf{e}_v(\lambda) &= (0, 0, 1)^{\mathrm{T}} \\ \mathbf{e}_w(\lambda) &= (\cos\lambda, \sin\lambda, 0)^{\mathrm{T}}. \end{aligned} \tag{2}$$

During the scan, the plane of the detector is spanned by the axes $\mathbf{e}_u(\lambda)$ and $\mathbf{e}_v(\lambda)$ and is at fixed distance D from the source. In order to address any given location on this detector, we use coordinates $u \in [-u_m, u_m]$ and $v \in [-v_m, v_m]$ that are measured along these two axes, $\mathbf{e}_u(\lambda)$ and $\mathbf{e}_v(\lambda)$, respectively. The coordinate origin $(u, v)^{\mathrm{T}} = (0, 0)^{\mathrm{T}}$ is set to the orthogonal projection of $\mathbf{a}(\lambda)$ onto the detector; see Fig.1.

Let $f(\mathbf{x})$ denote the spatial distribution of the X-ray linear attenuation coefficient of the object interrogated with the described CT device. This object is assumed to fit entirely in a cylinder of circular base that is centered on the z-axis and has radius $R_0 < R$. Consequently, $f(\mathbf{x}) = 0$ for all points with $\sqrt{x^2 + y^2} > R_0$. CB data acquisition yields ray integrals of the object density that can be expressed as

$$g(\lambda, u, v) = \int_0^\infty dt\, f(\mathbf{a}(\lambda) + t\boldsymbol{\alpha}(\lambda, u, v)) \tag{3}$$

where

$$\boldsymbol{\alpha}(\lambda, u, v) = \frac{u\,\mathbf{e}_u(\lambda) + v\,\mathbf{e}_v(\lambda) - D\,\mathbf{e}_w(\lambda)}{\sqrt{u^2 + v^2 + D^2}} \tag{4}$$

is a unit vector in the direction of the ray that starts at $\mathbf{a}(\lambda)$ and intersects the detector at coordinates $(u, v)^{\mathrm{T}}$. For a fixed λ, the function $g(\lambda, u, v)$ describes one single CB projection of the interrogated object with the vertex position at $\mathbf{a}(\lambda)$. In the following, we assume that the detector dimension in u is large enough to avoid, for each $\lambda \in [0, 2\pi)$, transaxial truncation in the acquired CB projection. This means that $g(\lambda, u, v) = 0$ for $|u| > u_m$. On the other hand, we consider objects that have large extent in axial direction, so that data truncation along the coordinate v is an immanent feature of the acquired CB projections.

III. Reconstruction Theory

The reconstruction problem in the described CB geometry corresponds to recovering values of the function $f(\mathbf{x})$ from the acquired CB projections, $g(\lambda, u, v)$, with $\lambda \in [0, 2\pi)$, $u \in [-u_m, u_m]$ and $v \in [-v_m, v_m]$. In this work, we suggest to reconstruct

$$\hat{f}(\mathbf{x}) = -\frac{1}{4\pi}\int_0^{2\pi} d\lambda\, \frac{1}{R - \mathbf{x}\cdot\mathbf{e}_w(\lambda)} g_F\left(\lambda, u^*(\lambda), v^*(\lambda)\right) \tag{5}$$

as an approximation of $f(\mathbf{x})$. Here and in the following, we use the dot to denote an inner product and we use a superscript $*$ to denote, without explicitly listing its argument, any function that depends on $\mathbf{x}$. In expression (5), $g_F(\lambda, u, v)$ denotes some filtered CB data, and $u^*(\lambda)$ and $v^*(\lambda)$ give the coordinates of the CB projection of $\mathbf{x}$ onto the detector plane at source position λ. These coordinate values are given as

$$u^*(\lambda) = \frac{D\mathbf{x}\cdot\mathbf{e}_u(\lambda)}{R - \mathbf{x}\cdot\mathbf{e}_w(\lambda)} \text{ and } v^*(\lambda) = \frac{D\mathbf{x}\cdot\mathbf{e}_v(\lambda)}{R - \mathbf{x}\cdot\mathbf{e}_w(\lambda)}. \tag{6}$$

Hence, image reconstruction is achieved by a weighted CB backprojection of filtered CB data. This data is defined as

$$\begin{aligned} g_F\left(\lambda, u^*, v^*\right) = \frac{1}{2}\int_{-\infty}^{\infty} du\, \frac{1}{\pi(u^*(\lambda) - u)} \\ \times \left(\tilde{g}^e\big(\lambda, u, v_A^*(\lambda, u)\big) + \tilde{g}^e\big(\lambda, u, v_B^*(\lambda, u)\big)\right), \end{aligned} \tag{7}$$

where

$$v_A^*(\lambda, u) = v^*(\lambda) + m_A^*(\lambda)(u - u^*(\lambda)), \tag{8}$$

$$v_B^*(\lambda, u) = v^*(\lambda) + m_B^*(\lambda)(u - u^*(\lambda)) \tag{9}$$

and where the singularity at $u^*(\lambda) = u$ is handled as a principal value of Cauchy. Equation (7) describes the average of the outcome at $u^*(\lambda)$ of two 1D convolutions of values of $\tilde{g}^e(\lambda, u, v)$ with the Hilbert filter kernel. These convolutions

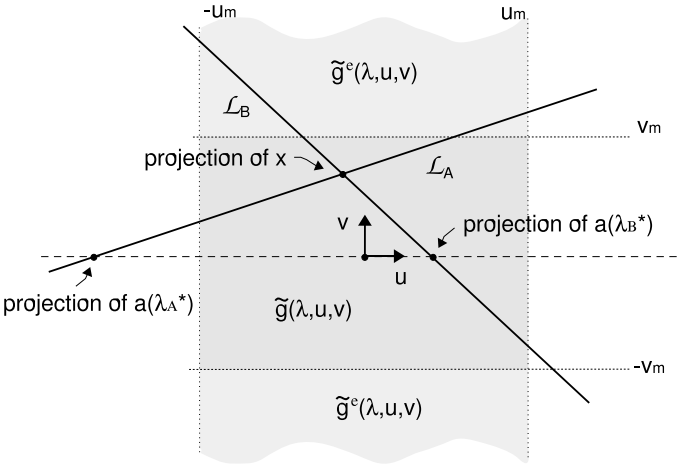

Fig. 2. The filter lines $\mathcal{L}_A$ and $\mathcal{L}_B$ required for reconstruction at $\mathbf{x}$ are defined by the lines connecting the CB projection of $\mathbf{x}$ with the CB projection of $\mathbf{a}(\lambda_A^*)$ or $\mathbf{a}(\lambda_B^*)$, respectively. The differentiated and weighted CB data function $\tilde{g}$, which is supported in $v \in [-v_m, v_m]$ and $u \in [-u_m, u_m]$ (dark region), is constantly extrapolated in v to yield the function $\tilde{g}^e$. The extrapolated function, $\tilde{g}^e$, has infinite support in v (indicated by the bright region), which avoids the issue of axial data truncation along the filter lines.

are computed along filter lines $\mathcal{L}_A$ and $\mathcal{L}_B$, the slopes of which are respectively given as $m_A^*(\lambda) = m_B^*(\lambda) = 0$ if $v^* = 0$, and otherwise as

$$m_A^*(\lambda) = \frac{(\mathbf{x} - \mathbf{a}(\lambda_A^*)) \cdot \mathbf{e}_v(\lambda)}{(\mathbf{x} - \mathbf{a}(\lambda_A^*)) \cdot \mathbf{e}_u(\lambda)} \quad (10)$$

$$m_B^*(\lambda) = \frac{(\mathbf{x} - \mathbf{a}(\lambda_B^*)) \cdot \mathbf{e}_v(\lambda)}{(\mathbf{x} - \mathbf{a}(\lambda_B^*)) \cdot \mathbf{e}_u(\lambda)}, \quad (11)$$

with $\lambda_A^* \in [0, 2\pi)$ and $\lambda_B^* \in [0, 2\pi)$.

By definition, the two filter lines contain each the point $(u^*(\lambda), v^*(\lambda))^{\mathrm{T}}$, but also the CB projection of the point $\mathbf{a}(\lambda_A^*)$ (for line $\mathcal{L}_A$) or $\mathbf{a}(\lambda_B^*)$ (for line $\mathcal{L}_B$) onto the plane of the detector; see Fig. 2 for an illustration. The parameters λ_A^* and λ_B^* can be selected arbitrarily and may also depend on $\mathbf{x}$, as implied with our notation; the actual choice of λ_A^* and λ_B^* plays a crucial role in the performance of the reconstruction algorithm, as will be explained in Sec. IV. The singularities that appear in the right hand side integral of (5) when $\left(\mathbf{x} - \mathbf{a}(\lambda_{A/B}^*)\right) \cdot \mathbf{e}_u(\lambda)$ becomes 0 are handled in the sense of Cauchy principal value; these singularities occur when filter lines become vertical on the detector plane.

The function $\tilde{g}^e(\lambda, u, v)$ in (7) is defined as

$$\tilde{g}^e(\lambda, u, v) = \begin{cases} D\tilde{g}(\lambda, u, -v_m)/\sqrt{u^2 + v_m^2 + D^2} & \text{if } v < -v_m \\ D\tilde{g}(\lambda, u, v_m)/\sqrt{u^2 + v_m^2 + D^2} & \text{if } v > v_m \\ D\tilde{g}(\lambda, u, v)/\sqrt{u^2 + v^2 + D^2} & \text{otherwise.} \end{cases} \quad (12)$$

where $\tilde{g}$ denotes the result of differentiating the CB data with respect to λ at fixed ray direction. Hence, the function $\tilde{g}^e(\lambda, u, v)$ is obtained from differentiated and weighted CB data by a constant extrapolation in v of the values at coordinates v_m and $-v_m$. This extrapolation avoids that an evaluation of differentiated CB data along the lines $\mathcal{L}_A$ or $\mathcal{L}_B$ experiences data truncation issues whenever these filter lines exceed the support of $\tilde{g}(\lambda, u, v)$ in v-direction; see also [4] for more details.

IV. Cone-Beam Artifacts and the Z-smart Method

The Z-smart reconstruction algorithm defined by (5)-(12) allows numerically-stable and CB artifact-free reconstruction at a point $\mathbf{x}$ in the following cases:

(i) If $\mathbf{x}$ belongs to the plane of the circle scan.

(ii) If the density function to be reconstructed is entirely independent of z, i.e., if $f(\mathbf{x}_1) = f(\mathbf{x}_2)$ for $\mathbf{x}_1 = (x, y, z_1)$ and $\mathbf{x}_2 = (x, y, z_2)$ with x, y, z_1 and z_2 all arbitrary.

(iii) If $\mathbf{x}$ belongs to the plane $\mathcal{P}$ that contains $\mathbf{a}(\lambda_A^*)$ and $\mathbf{a}(\lambda_B^*)$ and that is orthogonal to the source-trajectory plane, and if the object density function is independent of z within this plane, i.e., if $f(\mathbf{x}_1) = f(\mathbf{x}_2)$ for $\mathbf{x}_1 = (x, y, z_1) \in \mathcal{P}$, $\mathbf{x}_2 = (x, y, z_2) \in \mathcal{P}$ with x, y, z_1 and z_2 all arbitrary.

Postulate (i) goes along with our expectations and can be illustrated easily. The CB projection of any point $\mathbf{x} = (x, y, 0)^{\mathrm{T}}$ onto the detector plane has coordinate $v^*(\lambda) = 0$ for all λ, according to (6). The slopes of the filter lines required by the Z-smart method for reconstruction at any such point are therefore given as $m_A^*(\lambda) = m_B^*(\lambda) = 0$ for each CB projection. Consequently, each occurring filter line has equation $v = 0$, so that data filtering only involves CB data for rays that are entirely contained in the source-trajectory plane. Hence, for points in the plane of the circle scan, the reconstruction problem in our geometry reduces to the 2D fan-beam reconstruction problem and the Z-smart method reduces to the fan-beam filtered-backprojection formula of Noo *et al.* [5], which yields theoretically-exact reconstruction results.

Postulate (iii) states the main result of this paper, namely that the reconstruction in the vertical plane $\mathcal{P}$ will be free of CB artifacts if the function f is z-invariant within $\mathcal{P}$ and if the two points, $\mathbf{a}(\lambda_A^*)$ and $\mathbf{a}(\lambda_B^*)$, both belong to $\mathcal{P}$. The proof of this case is somewhat more lengthy and is based on relating the Z-smart method to the theoretically-exact reconstruction approach from [6].

On the other hand, the validation of postulate (ii) is straightforward, since it follows directly as a special case of (iii).

Note that FDK allows stable reconstruction without CB artifacts in cases (i) and (ii), but not in case (iii).

V. Selection of Filter Parameters

As described in Sec. III, the Z-smart reconstruction method involves the selection of parameters, λ_A^* and λ_B^*, that affect the filtering step during image reconstruction. In general, these parameters may be selected individually for each point in the image domain, as mentioned earlier and emphasized by the superscript $*$.

We now suggest a specific selection of these parameters that aims at minimizing the impact of CB artifacts on the reconstruction results. More specifically, we would like to determine, for as many points $\mathbf{x}$ as possible, values of λ_A^* and λ_B^*, such that the requirements of postulate (iii) from the previous section apply. In other words, we would like to find a vertical slice through $\mathbf{x}$ in which the density function is z-independent and use the polar angles of the two intersections of this slice with the source trajectory to define $\lambda_A(\mathbf{x})$ and $\lambda_B(\mathbf{x})$. If such a plane can be found, reconstruction at $\mathbf{x}$ will be CB artifact free, according to (iii) from Sec. IV.

Technically, finding such a plane requires some a priori information about the interrogated object, namely the knowledge of the general homogeneity distribution within vertical slices of the object. This information is here estimated in a preprocessing step, directly from the CB data function g. Our estimation involves the following homogeneity criterion:

$$c(\mathbf{x}, \lambda_1) = \left[\int_{-v_m}^{v_m} dv \left(\frac{\partial}{\partial v} \frac{D\, g(\lambda_1, u^*(\lambda_1), v)}{\sqrt{u^{*2}(\lambda_1) + v^2 + D^2}} \right)^2 \right]^{\frac{1}{2}} + \left[\int_{-v_m}^{v_m} dv \left(\frac{\partial}{\partial v} \frac{D\, g(\lambda_c, u^*(\lambda_c), v)}{\sqrt{u^{*2}(\lambda_c) + v^2 + D^2}} \right)^2 \right]^{\frac{1}{2}}. \quad (13)$$

with

$$\lambda_c = \lambda_1 + \pi - 2\,\mathrm{atan}(u^*(\lambda_1)/D). \quad (14)$$

To understand this criterion, focus first on the vertical plane $\mathcal{P}$ through the points $\mathbf{a}(\lambda_1)$ and $\mathbf{x}$, as depicted in Fig. 3 and

note that the selection of λ_c in (14) assures that $\mathcal{P}$ also contains the point $\mathbf{a}(\lambda_c)$. At each of the two source positions, $\mathbf{a}(\lambda_1)$ and $\mathbf{a}(\lambda_c)$, the projection of P onto the detector is a vertical line (drawn at $u = u^*(\lambda_1)$ or $u = u^*(\lambda_c)$, resp.) and the criterion in (ii) evaluates the behavior of g on this line. This means in particular that the calculation of $c(\mathbf{x}, \lambda_1)$ involves only data on the rays that are within $\mathcal{P}$. Consider now the first term of $c(\mathbf{x}, \lambda_1)$, which gives, for the CB projection acquired at λ_1, the L_2-norm of v-differentiated CB data at coordinate $u^*(\lambda_1)$. Assuming that f is z-independent in $\mathcal{P}$, we can find that

$$
\begin{aligned}
&\frac{\partial}{\partial v}\frac{Dg(\lambda_1, u^*(\lambda_1), v)}{\sqrt{u^{*2}(\lambda_1) + v^2 + D^2}} \\
&= \frac{\partial}{\partial v}\left\{ \frac{D}{\sqrt{u^{*2}(\lambda_1) + v^2 + D^2}} \right. \\
&\qquad \left. \times \int_0^\infty dt\, f\Big(\mathbf{a}(\lambda_1) + t\boldsymbol{\alpha}(\lambda_1, u^*(\lambda_1), v\Big) \right\} \\
&= \frac{\partial}{\partial v}\left\{ D \int_0^\infty dt\, f\Big(\mathbf{a}(\lambda_1) + tu^*(\lambda_1)\mathbf{e}_u(\lambda_1) \right. \\
&\qquad \left. + tv\mathbf{e}_v(\lambda_1) - tD\mathbf{e}_w(\lambda_1)\Big) \right\} \\
&= \frac{\partial}{\partial v}\left\{ D \int_0^\infty dt\, f\Big(\mathbf{a}(\lambda_1) + tu^*(\lambda_1)\mathbf{e}_u(\lambda_1) - tD\mathbf{e}_w(\lambda_1)\Big) \right\} \\
&= 0.
\end{aligned}
\tag{15}
$$

Hence, the first term in $c(\mathbf{x}, \lambda_1)$ will yield 0 if the object density is z-independent in $\mathcal{P}$. (The step from line 3 to line 4 in (15) uses our z-independent assumption and the fact that $\mathbf{e}_v(\lambda_1)$ is parallel to the z-axis.) A similar derivation shows that under this assumption, the second term necessarily also yields 0.

Although none of the two terms in c corresponds to a sufficient condition, we here hypothesize that the function $c(\mathbf{x}, \lambda_1)$ gives an indication of the z-homogeneity of the object in the vertical plane through $\mathbf{a}(\lambda_1)$, $\mathbf{a}(\lambda_c)$ and $\mathbf{x}$. Following our hypothesis, we thus assume that the requirements for an application of postulate (iii) for CB artifact free reconstruction within this plane will be satisfied if $c(\mathbf{x}, \lambda_1) = 0$.

For each point $\mathbf{x}$ where reconstruction is to be achieved, we determine the parameter λ_1 that minimizes $c(\mathbf{a}, \lambda_1)$ and use $\lambda_A(\mathbf{x}) = \lambda_1$ and $\lambda_B(\mathbf{x}) = \lambda_c$ to define the filter parameters used for reconstruction. Note that in the numerical implementation of the Z-smart algorithm, this minimization corresponds to a simple search operation and can be achieved very efficiently.

VI. Numerical Evaluation

We now present a numerical evaluation of the Z-smart reconstruction method defined in Sec. III, while using the specific selection of the filter parameters suggested in Sec. V. Our computer-based studies involved an analytically defined tube phantom, which consists of eight stacks of high-attenuating disks (each disk has density 1000HU) enclosing a central, long cylinder of radius 10cm. The bottom edge of each disk-stack is 5mm below PCS, and the axis of the central cylinder is along the z-axis. We assumed that the task was to image

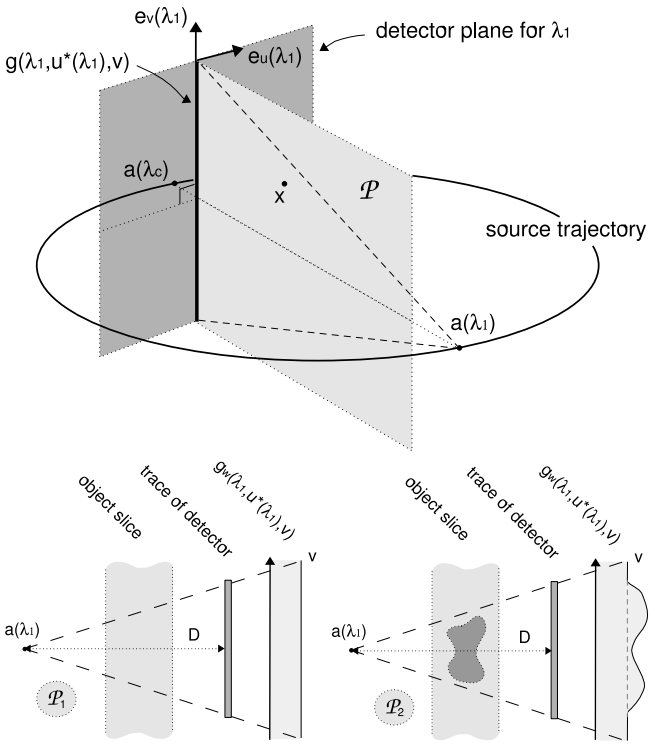

Fig. 3. (Top) The criterion for estimating the homogeneity in the vertical plane $\mathcal{P}$, as defined in equation (13), is based on two terms, each of which yields an individual homogeneity estimate by involving the CB data samples $g(\lambda_1, u^*(\lambda_1), v)$ (or $g(\lambda_c, u^*(\lambda_c), v)$). (Bottom) Illustration of the weighted CB data $\frac{D\, g(\lambda_1, u^*(\lambda_1), v)}{\sqrt{u^{*2}(\lambda_1) + v^2 + D^2}}$, here abbreviated as $g_w(\lambda_1, u^*(\lambda_1), v)$, for two different cases: (left) for the slice $\mathcal{P}_1$, in which the object density is z-homogeneous, and for the slice $\mathcal{P}_2$, in which the object density is not z-homogeneous.

TABLE I

CB data simulation parameters

	FDK, Z-smart	ART
radius of trajectory [mm]	$R = 500$	$R = 500$
distance source-detector [mm]	$D = 1000$	$D = 1000$
projections per full scan	1160	580
detector pixel width [mm]	$\Delta u = 1.0$	$\Delta u = 2.0$
detector pixel height [mm]	$\Delta v = 1.0$	$\Delta v = 2.0$

the content of the central cylinder; hereafter, this content is called the region-of-interest (ROI). This ROI has background density of 0HU and may contain varying structures, such as embedded low- or high-contrast inlays. Three distinct versions of the tube phantom were considered, see Fig. 4. We refer to these versions as the uniform tube phantom, the low-contrast tube phantom and the high-contrast tube phantom.

We simulated CB data of the three tube phantoms using the geometry and discretization parameters listed in table I. For the uniform tube phantom, we also simulated noisy CB data by assuming a Poisson noise model and an emission of $25,000$ photons per ray. In the considered acquisition geometry, the eight stacks of disks completely projected into the measured detector region for each λ. The projection of the central cylinder, however, exceeded the detector in v during the entire simulated scan.

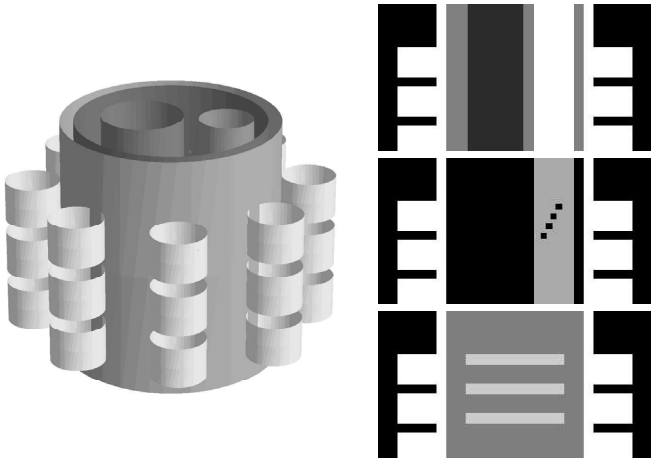

Fig. 4. (Left) 3D illustration of the general structure of the involved tube phantoms. (Right) The slice $y = 0$mm through the three considered tube phantom versions, presenting a closer view on the different contents of the ROI. (top) the uniform tube phantom (grayscale window [-300HU,300HU]), (center) the high-contrast tube phantom in [-50HU,550HU], (bottom) the low-contrast tube phantom in [-100HU,100HU]

Using the Z-smart method, we then carried out image reconstruction from the simulated CB data sets on an isotropic, Cartesian sampling grid with a sample spacing of $\Delta x = \Delta y = \Delta z = 1$mm. Our reconstruction algorithm was evaluated on its capability to accurately recover the object density in the ROI. Obviously, the general difficulty of this task is given by the strong density variations in z of the phantom within the stacks of disks. On the other hand, these stacks are localized in x and y and, in particular, located entirely outside the ROI. To facilitate the assessment of image quality, we also performed reconstructions using two other, state-of-the-art CB reconstruction methods, namely the FDK approach [3] and the algebraic reconstruction technique (ART) [7]. The ART is of special interest here, since - unlike FBP-type algorithms - it needs no algorithmic adaptation to the sampling path used. The FDK reconstruction was obtained by applying sinc-apodization to the ramp-filter kernel. For the ART reconstruction, we carried out 10 iterations, starting with an empty image volume. The iterative update was performed projection-wise, with an increment-step of 100 projections and a relaxation factor of 0.1. No additional constraints were used. Forward projection used ray-tracing, integrating along the rays in steps of 0.5 voxels using trilinear interpolation between nearest voxel neighbours. For backprojection, we used standard voxel-driven CT backprojection with bilinear interpolation on the detector. We temporarily refined the volume sampling grid by a factor of 2 in each dimension during the reconstruction. The final ART-sampling grid equaled the grid used for the FBP.

Figure 5 presents the vertical slice $y = 0$mm through the reconstructions of the uniform as well as of the low-contrast disc phantom, obtained from non-noisy CB data with FDK, ART and the Z-smart reconstruction methods. Figure 6 compares the slices $y = 0$mm through the FDK and Z-smart reconstructions of the high-contrast tube phantom (ontained with noise-free CB data) and of the uniform tube phantom (with added noise assuming $25,000$ photons per ray). Some representative transaxial slices through the reconstructions of

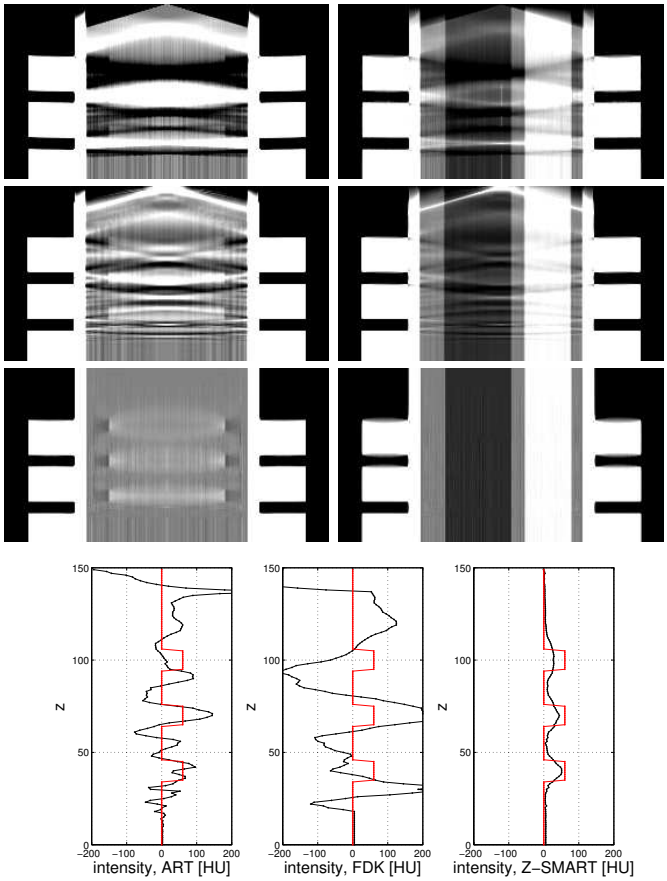

Fig. 5. The slices $y = 0$mm through the reconstructions of the (left) uniform and the (right) low-contrast tube phantom: (Top) using full-scan FDK, (center) using ART and (bottom) using the Z-smart reconstruction algorithm. Visualization in (left) [-100HU,+100HU] and (right) [-300HU,+300HU]. The graph at the bottom shows the reconstructed densities of the low-contrast tube phantom along the vertical profile at $(x, y) = (-40, 0)$mm (black), compared to the true density values (red).

the uniform and the low-contrast phantom versions are shown in Fig. 7.

Our results show that the CB artifacts caused by the localized stacks of high-attenuating discs appear significantly different in the evaluated reconstruction methods: In the FDK

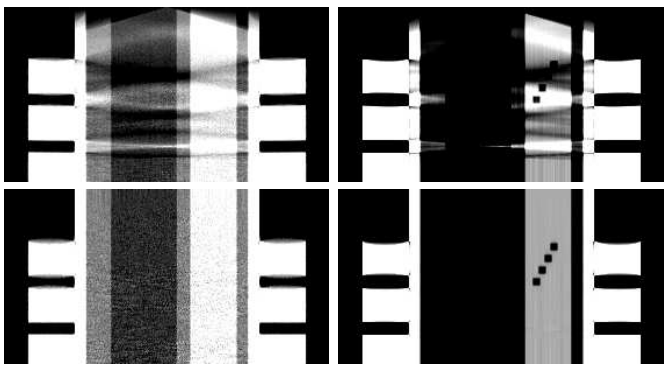

Fig. 6. The slices $y = 0$mm through the reconstructions of (left) the uniform tube phantom while using noisy CB data (grayscale [-300HU,+300HU]) and (right) the high-contrast tube phantom while using non-noisy data ([-50HU,+550HU]): (Top) using full-scan FDK, (bottom) using the Z-smart reconstruction method.

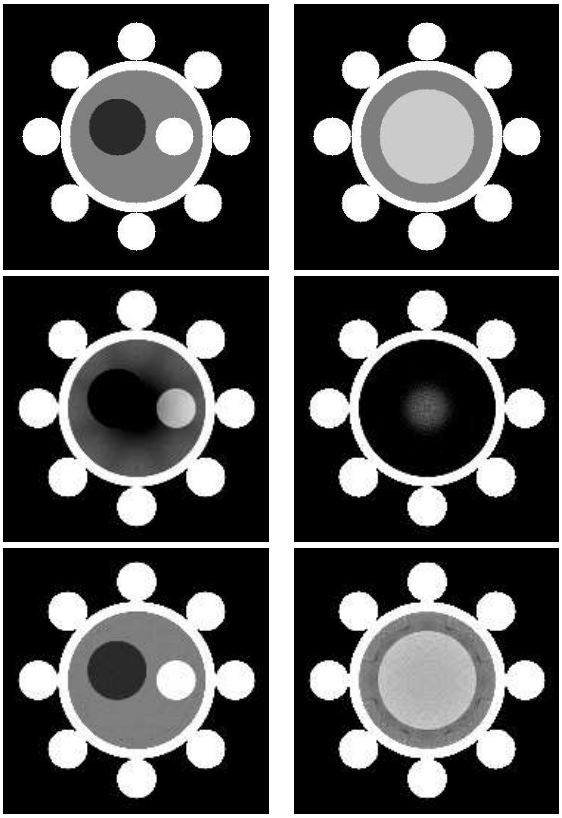

Fig. 7. Visualization of the transaxial slices (left) $z = 90$mm through the reconstruction of the original tube phantom in $[-300HU, 300HU]$ and (right) $z = 40$mm through the reconstruction of the tube phantom with low contrast features in $[-100HU, 100HU]$. (Top to Bottom) true density values, (center) reconstruction using full-scan FDK, (bottom) reconstruction using the Z-smart method.

reconstructions, these artifacts spread over large areas of the object, so that an interpretation of the interior structure of the tube phantom is very difficult, if not impossible (see top row of figures 5 and figures 6). Furthermore, these artifacts cause a significant shift in the reconstructed density values; see the transaxial cross-sections shown in Fig. 7.

The artifacts occurring in the ART reconstructions are of similar structure and support, however of noticable reduced intensity when compared to these of the FDK reconstructions. But still, image quality obtained with ART within the ROI is not entirly satisfying. The Z-smart method, however, effectively restricts the CB artifacts to the regions of the disk stacks, so that these artifacts do not affect the rather homogeneous interior regions of the phantom. Overall image quality inside the ROI is significantly improved in the results of the Z-smart method and now, for instance, the disc inlays of the low-contrast tube phantom can be distinguished easily (see the profile at the bottom of Fig. 5). Reconstructions from noisy CB data, as presented in Fig. 6, verify the numerical stability of the Z-smart algorithm, which seems to be comparable to that of FDK (at least, by visual inspection).

VII. Discussion and Conclusions

In this paper, we suggested a novel, Z-smart, approach for image reconstruction from CB data corresponding to a full circular scan. The object density at any arbitrary point is recovered via 1D filtering of differentiated CB data along two filter directions and subsequent 3D CB backprojection of the filtered data.

The filter directions depend on two parameters, λ_A^* and λ_B^*, that may be defined individually for each point in the image volume and that allow great control on achievable image quality. We showed that a proper selection of these parameters can yield CB artifact free reconstruction within a vertical slice of the object, if the object density is z-independent within this slice.

At the same time, the selection of λ_A^* and λ_B^* also affects the computational complexity of the Z-smart reconstruction formula. For instance, considering a realization for which λ_A^* and λ_B^* are invariant with respect to $\mathbf{x}$ results in an efficient algorithm that follows the classical filtered-backprojection scheme. A voxel-dependent definition of these parameters – such as the one used in Sec. V – yields in general shift-variant filter operations and a computationally less efficient algorithm, but provides great control on the appearance of CB artifacts. Hence, the selection of λ_A^* and λ_B^* requires a trade-off between efficiency and accuracy. We here focused on maximizing achievable image quality and suggested to select these parameters by involving a criterion for efficiently estimating the homogeneity distribution of the object in a preprocessing step. This criterion provides a necessary, but not sufficient way of testing the z-uniformity of the object density in any vertical slice, but proved to work well in all considered experiments.

The numerical evaluation demonstrates that the suggested realization of the Z-smart algorithm can, in certain scenarios, significantly reduce CB artifacts in comparison to the FDK method, but also to a fully 3D iterative reconstruction approach (ART). This is especially the case when imaging objects that contain structures with strong density variations along z, which are, however, localized in x and y. Whereas both, FDK and ART, distribute the CB artifacts caused by these localized heterogeneities over large parts of the image, the Z-smart method allows these artifacts to be constricted near the regions where they originate from.

The reconstruction approach we presented in this paper can also be applied when considering planes that are not perpendicular to the plane of the source trajectory. Considering these more flexible scenarios might require some additional effort in the preprocessing operations, such as the application of a more complex homogeneity criterion, but might also yield further improvements in achievable image quality.

Acknowledgement

The authors would like to thank Holger Kunze, Siemens AG, Medical Solutions, Forchheim, Germany for providing an implementation of the ART method.

Disclaimer

The concepts and information presented in this paper are based on research and are not commercially available.

REFERENCES

[1] H. K. Tuy, "An inversion formula for cone beam reconstruction," *SIAM J. Appl. Math.*, vol. 43, no. 3, pp. 546–552, 1983.

[2] D. V. Finch, "Cone beam reconstruction with sources on a curve," *SIAM J. Appl. Math.*, vol. 45, no. 4, pp. 665–673, 1985.

[3] L. A. Feldkamp, L. C. Davis, and J. W. Kress, "Practical cone-beam algorithm," *J. Opt. Soc. Am. A*, vol. 1, no. 6, pp. 612–619, 1984.

[4] S. Hoppe, J. Hornegger, G. Lauritsch, F. Dennerleien, and F. Noo, "Truncation correction for non-horizontal filter lines," in *Proceedings of the Fully3D*, Lindau, Germany, 2007, pp. 209–212.

[5] F. Noo and D. J. Heuscher, "Image reconstruction from cone-beam data on a circular short-scan," in *Proceedings of the SPIE*, vol. 4684, San Diego, CA, USA, 2002, pp. 50–59.

[6] J. D. Pack and F. Noo, "Cone-beam reconstruction using 1D filtering along the projection of M-lines," *Inverse Problems*, vol. 21, pp. 1105–1120, 2005.

[7] F. Natterer and F. Wübbeling, *Mathematical Methods in Image Reconstruction*. SIAM, 2001.